Optimization of the design and microfabrication of a biologically inspired nano-aerial flapping wing vehicle

Marguerite de La Bigne, Eric Cattan, Ahmad Itawi, Sofiane Ghenna, Sébastien Grondel, Olivier Thomas

To cite this version:

Marguerite de La Bigne, Eric Cattan, Ahmad Itawi, Sofiane Ghenna, Sébastien Grondel, et al.. Optimization of the design and microfabrication of a biologically inspired nano-aerial flapping wing vehicle. IEEE-NEMS, May 2024, Kyoto, Japan. ⟨10.1109/NEMS60219.2024.10639904⟩. ⟨hal-04703860⟩

HAL Id: hal-04703860
https://hal.science/hal-04703860v1

Submitted on 25 Oct 2024

Optimization of the design and microfabrication of a biologically inspired nano-aerial flapping wing vehicle

de La Bigne Marguerite
Univ. Polytechnique Hauts-de-France
IEMN, CNRS, Univ. Lille, UMR 8520
Lille, France
marguerite.de_la_bigne@ensam.eu

Cattan Éric
Univ. Polytechnique Hauts-de-France
IEMN, CNRS, Univ. Lille, UMR 8520
Lille, France
eric.cattan@uphf.fr

Itawi Ahmad
Univ. Polytechnique Hauts-de-France
IEMN, CNRS, Univ. Lille, UMR 852
Lille, France
ahmad.itawi@uphf.fr

Ghenna Sofiane
Univ. Polytechnique Hauts-de-France
IEMN, CNRS, Univ. Lille, UMR 8520
Lille, France
sofiane.Ghenna@uphf.fr

Grondel Sébastien
Univ. Polytechnique Hauts-de-France
IEMN, CNRS, Univ. Lille, UMR 8520
Lille, France
sebastien.grondel@uphf.fr

Thomas Olivier
Arts et Métiers Institute of Technology
LISPEN, HESAM Université
Lille, France
olivier.thomas@ensam.eu

***Abstract*—Insects are characterized by their agility in flight, including hovering, backward and forward movements. Studies on insect flight have revealed that the lifting force generated by vibrating wings is most effectively produced when flapping and twisting movements are in phase quadrature, *i.e.* one being maximal when the other is zero. Based on these results, Nano Air Vehicles (NAV) that replicate insect wing motion using a fully flexible structure were fabricated through microfabrication using lithography methods. In this article, we will show that it is possible to design more efficient vibrating wings by replacing their fully flexible ribs with an assembly of thin and thick parts, the former constituting the compliant links and the latter composing the rigid bodies. The first advantage of this concept is that the wing optimisation can be carried out on a simple mass/spring vibrating systems with very few degrees of freedom. Another advantage is that these prototypes are more resistant because the thinness of the structure is concentrated at the compliant link. This means that very high vibration amplitudes can be achieved without damaging the structure.**

***Index Terms*—Resonant motion, Micro/Nano electromechanical system (M/NEMS), Modal combination, Design of structural vibration, Optimization, Compliant links**

I. INTRODUCTION

Understanding of insect flight has improved considerably and it has been shown that lift force results both from a wide range of unconventional aerodynamic mechanisms [1] and from specific kinematics induced by the thorax and flexible characteristics of the wings [2]. Since the kinematics can be approximated by a combination of twisting and flapping movements [3]–[5], some research projects are using this principle to build unmanned air vehicles (UAVs) that mimic the kinematics of an insect wing [6], [7].

In this article, we focus on the smallest category of UAVs, those weighing less than $10\,\mathrm{g}$, the nano-air vehicles (NAVs) [8]–[12]. In the literature, there are two main approaches to the design and manufacturing of NAV wings: one is to develop rigid wings coupled to a 4-bar system to amplify movement [8], [9] using 3D printing, while the other, applied by our team, is to design fully flexible structures using microfabrication technology [12], [13]. Compared with the state of the art, the use of microfabrication enables very light and small prototypes to be produced as well as massive production at low cost.

The NAV is a vibrating structure with two resonant modes: the flapping mode and the twisting mode [15]. The design of these flexible structures is determined by their modal properties. The flapping mode (Fig. 1 (b)) occurs when the leading and trailing edges are in phase, while the twisting mode (Fig. 1 (c)) corresponds to the frequency at which they are out of phase. As a result, the movement of the NAV can be described as a combination of these two modes, as shown in Fig. 1 (a) where the frequency response function (FRF) is for each frequency the displacement at a specific point divided by the applied force. The orange solid line represents the combined FRF for the leading edge end of the first mode (purple solid line in Fig. 1 (a)) and the second mode (turquoise solid line in Fig. 1 (a)). The kinematics of insect flight is considered optimal when the flapping and twisting modes are in phase quadrature, *i.e.* when one is maximum when the other one is minimal (Fig. 1 (d)) and that large displacements can be obtain. This implies to set the dimensions of the NAV in order to bring the two modes as close as possible. However the design and optimisation of a fully flexible structure is still complex do to the large number of parameters to be analysed.

To address this issue, this article proposes a new design methodology for the NAV by replacing the fully flexible

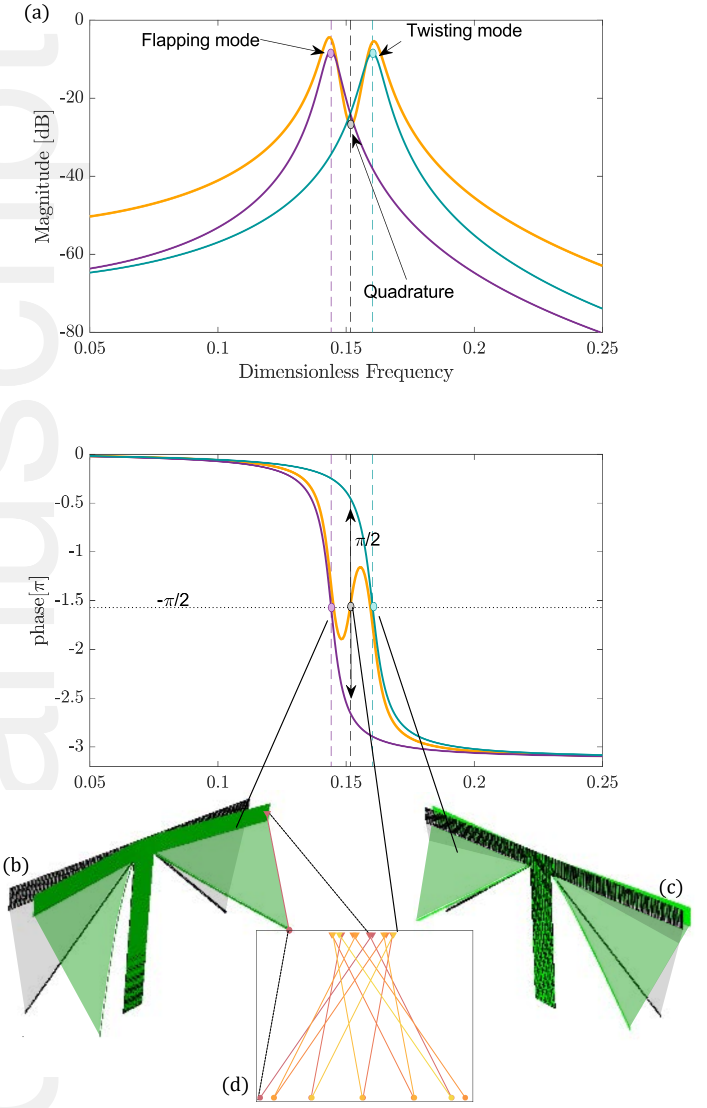

Fig. 1. (a) Frequency response function (FRF) for a NAV with flapping (b) and twisting (c) mode examples and (d) wing-edge motion at the quadrature

structure with rigid bodies and compliant links [14]. Therefore, this considerably reduces the number of variables used to size the NAV, making it much easier to optimise. Moreover the fabricated prototype will be more resistant because the thinness of the structure will be concentrated at the compliant link, allowing a very large vibration amplitude to be achieved without damaging the structure.

II. EQUIVALENCE PRINCIPLE

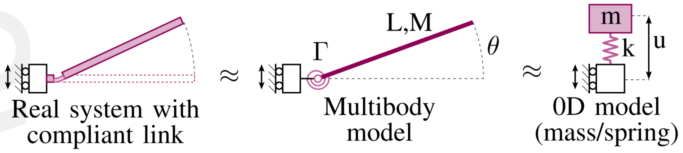

Fig. 2. Equivalent models for sizing the Nav

As mentioned in the introduction, the NAV geometries considered in this paper enable to concentrate the deformation in compliant links such that the optimization process relies on simple equivalent 0D models with very few degrees of freedom. To address this equivalence, we consider a system consisting of a single hinged rib and we examine the three models shown in Fig. 2.

The 0D model is a simple mass m / spring k system whose dynamics is governed by:

$$m\ddot{u} + ku = 0, \tag{1}$$

where $u(t)$ is the mass displacement and $\dot{u} = \mathrm{d}u/\mathrm{d}t$ its velocity.

The multibody model is composed of a rigid beam of mass M, length L and a torsional spring of stiffness Γ, such that:

$$\frac{L^2 M}{3}\ddot{\theta} + \Gamma\theta = 0, \tag{2}$$

where θ is the beam angle.

Comparing Eqs. (1) and (2), one shows that the two models are equivalent – *i.e.* they are governed by the same equation of motion – if one defines an equivalent length λ such that $u = \lambda\theta$. This leads to an equivalent mass and stiffness

$$m = \frac{LM}{3\lambda}, \quad k = \frac{\Gamma}{L\lambda}. \tag{3}$$

The choice for λ is arbitrary; one can choose $\lambda = L$ for instance, meaning that u corresponds to the tip displacement of the rigid beam in the multibody model.

The proposed real system is a single discontinuous beam of rectangular cross section, composed of two segments. The first, the rib, is of large thickness h and width b, with a length L. It is connected to the ground by a second thin segment, the compliant link, of thickness h_l, width b_l and length L_l. Since this system is fully deformable in bending, the equivalence of Fig. 2 is not exact and its behaviour will tend towards that of the multibody model if the thickness and the length of the rib are large compared with those of the compliant link, *i.e.* $h_l \ll h$ and $L_l \ll L$. In this case, neglecting the inertia of the compliant link segment, its equivalent torsional stiffness is as follows [14]:

$$\Gamma = \frac{EI_l}{L_l}, \tag{4}$$

where E is the material Young's modulus and $I_l = b_l h_l^3/12$ is the second moment of inertia of the cross section. To verify this conjecture, we rely on numerical simulations of the discontinuous beam using a finite-element software (Abaqus).

First we need to identify the number of independent parameters among the six on which the geometry of the discontinuous beam depends (h, b, L, h_l, b_l, L_l). We model the real system as an Euler-Bernoulli beam with variable cross section. Defining x as the position along the beam, $b(x), h(x)$ as the varying width and thickness, the transverse displacement $w(x,t)$ satisfies the following equation in free vibrations [18]:

$$\rho S\ddot{w} + (EIw'')'' = 0, \tag{5}$$

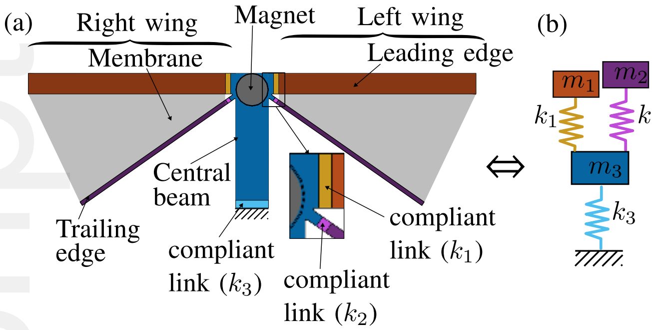

Fig. 3. Description of NAV and its equivalent 0D model

where $\dot{\circ} = \partial \circ / \partial t$ and $\circ' = \partial \circ / \partial x$, $S(x) = b_b(x) h_b(x)$ is the area of the section, $I(x) = b_b(x) h_b(x)^3/12$ is the second moment of area and ρ is the material density. This equation takes the form of:

$$\bar{b}\bar{h}\ddot{\bar{w}} + \left(\bar{b}\bar{h}^3\bar{w}''\right)'' = 0. \tag{6}$$

where

$$\begin{aligned} \bar{x} &= \frac{x}{L_l} \quad \bar{b} = \frac{b(x)}{b_l} \quad \bar{h} = \frac{h(x)}{h_l} \\ \bar{w} &= \frac{w}{L_l} \quad \bar{t} = \frac{t}{t_0} = t\frac{h}{L_l^2}\sqrt{\frac{E}{12\rho}}. \end{aligned} \tag{7}$$

This shows that for the two-segment beam considered, the free dynamics of the beam depends only on three free geometrical parameters, that can be defined as: b/b_l, h/h_l and L/L_l.

Comparison of the the first natural frequency of the real system and the natural frequency $\omega_0 = \sqrt{3\Gamma/(ML^2)}$ of the multibody model by finite element numerical simulations shows that the error between those two models both is less than 5% if $h/h_l > 8$ and $L/L_l > 16$, with b/b_l playing a negligible role. In practice, we always choose $b = b_l$. In conclusion, we consider that if those criteria are fulfilled, the equivalence between the real-system and the 0D model is verified, with m and k computed with Eqs. (3) and (4) with $M = bhL$.

III. NAV DESIGN AND OPTIMISATION

The designed NAV prototypes (see Fig.3 (a)), consist of two wings driven by an electromagnetic coil / magnet system. Here only the magnet is sketched but the coil is supposed to surround it. Each wing consists of two ribs, assumed to be rigid, with the leading edge and the trailing edge connected to the free end of the central beam by a compliant link. A very thin membrane is deposited between these edges to generate the thrust force of the NAV. The magnet positioned at the free end of a central beam, adjacent to the roots of the two wings, is subjected to an electromagnetic force generated by a coil, which may be internal or external. Acting as the motor of the NAV and fixed at its origin, the central beam is sufficiently flexible to enable the electromagnetic force to deform it, inducing a resonant movement of the two wings.

Based on the results of section II, we can approximate the NAV architecture with a 0D model, as illustrated in Fig. 3 (b). This equivalent model of one wing comprises three mass-spring systems. Each rib corresponds to a mass, denoted as m_1, m_2, and m_3, representing the leading edge, trailing edge, and central beam, respectively. The compliant link of those ribs is symbolized by the springs k_1, k_2, and k_3, respectively. In this configuration, the leading edge (depicted in orange) and trailing edge (depicted in purple) are connected to the central beam's free end. Consequently, in the equivalent 0D model, masses m_1 and m_2 are logically placed in parallel, both linked to mass m_3 in the 0D model.

To reduce the number of parameters to be optimised, the characteristic equation of this 0D model is rewritten in dimensionless form. Thus, by introducing the following dimensionless parameters:

$$\mu_3 = \frac{m_3}{m_1},\ \mu_2 = \frac{m_2}{m_1},\ \bar{\omega}_3 = \frac{\omega_3}{\omega_1},\ \bar{\omega}_2 = \frac{\omega_2}{\omega_1}, \tag{8}$$

where $\omega_i = \sqrt{\frac{k_i}{m_i}}$, is the angular natural frequency of the mass-spring system i, we obtain the following expressions for the mass and stiffness matrix, respectively:

$$\mathbf{M} = \begin{pmatrix} \mu_3 + 1 + \mu_2 & 1 & \mu_2 \\ 1 & 1 & 0 \\ \mu_2 & 0 & \mu_2 \end{pmatrix}, \quad \mathbf{K} = \begin{pmatrix} \mu_3\bar{\omega}_3^2 & 0 & 0 \\ 0 & 1 & 0 \\ 0 & 0 & \mu_2\bar{\omega}_2^2 \end{pmatrix}. \tag{9}$$

As explained in section I, we are looking for NAV geometries where the combination of flapping and twisting modes results in maximum amplitude at the phase quadrature frequency. However, as shown in Fig. 1 (a), the phase quadrature frequency is at an anti-resonance, which implies that, unlike resonance frequencies where motion is amplified, at anti-resonance, motion tends to be suppressed or significantly reduced. The most effective way to increase the anti-resonance amplitude is therefore to bring the frequencies of the two flapping and twisting modes as close together as possible. Furthermore, as the magnet is fixed at the end of the central beam, it is also crucial to ensure that its bending amplitude is not excessively large, in order to avoid collisions with the coil. This leads to two main optimization criteria: first to have two resonances as close together as possible and at the same amplitude, in order to increase the anti-resonance amplitude, second to have a ratio between the amplitude of the leading edge and the central beam of approximately 1/6.

The 0D model in Fig. 3 (b) has three modes as shown in Fig. 4: the flapping mode where m_1 and m_2 are in phase, the twisting mode, where m_1 and m_2, are in phase opposition and the central beam bending mode, where m_1 and m_2, are in phase opposition with m_3. The parameters that most influence the flapping and twisting modes are μ_2 and $\bar{\omega}_2$. To study them for the 0D model in Fig. 3 (b), the dimensionless pulsation $\bar{\omega}$ of the three modes (in different colors) as a function of $\bar{\omega}_2$ for several μ_2 (line styles) is plotted in Fig. 5. Here, $\bar{\omega}_3$ and μ_3 have been fixed to verify that m_3 has an amplitude approximately six times smaller than m_1 (second optimization

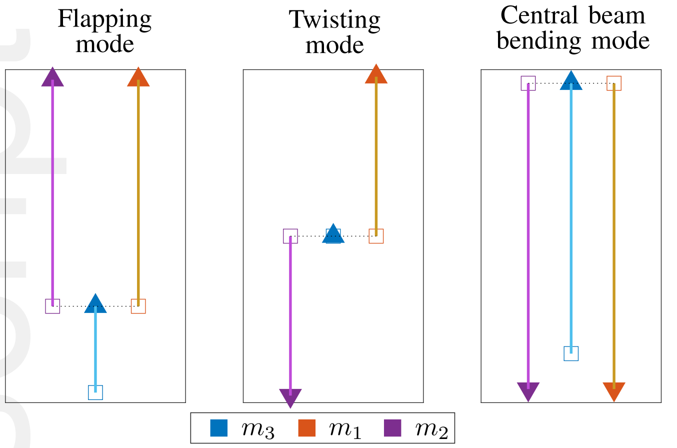

Fig. 4. Mode shapes of the equivalent 0D model. The white/colored markers denote the reference/deformation position of the masses respectively

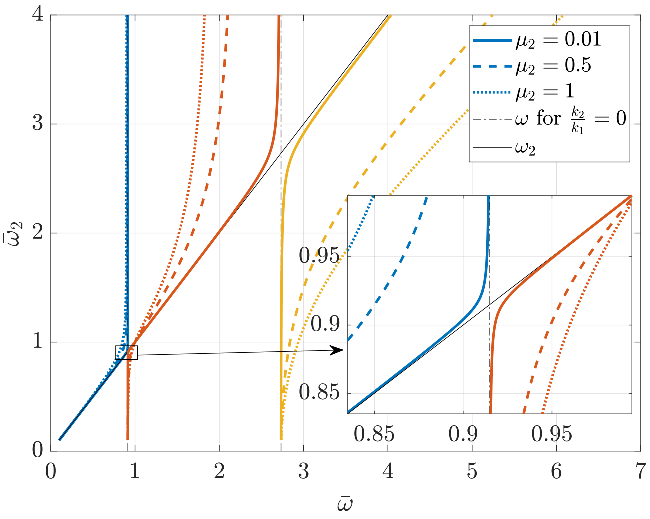

Fig. 5. Mode dimensionless pulsations analysis as a function of $\bar{\omega}_2$ and μ_2 for $\bar{\omega}_3 = 2.5$ and $\mu_3 = 0.95$

criterion). The blue and red solid lines in Fig. 5 represent the flapping and twisting mode respectively, while the yellow one represents the central beam bending mode. We can note that, according to Fig. 5, there is an optimal $\bar{\omega}_2$ for which the flapping and twisting modes are as close as possible. This corresponds to the angular frequency for the same 0D model with $k_2/k_1 = 0$, which can be expressed as a function of $\bar{\omega}_3$ and μ_3.

$$\bar{\omega}_{k_2-}^2 = \frac{\bar{\omega}_3^2+1}{2} + \frac{1}{2\mu_3} - \frac{\sqrt{\mu_3^2\left(\bar{\omega}_3^2-1\right)^2 + 2\mu_3\left(\bar{\omega}_3^2+1\right) + 1}}{2\mu_3} \tag{10}$$

More precisely, the difference between the dimensionless pulsations of the first two modes, $\bar{\omega}_+ - \bar{\omega}_-$, where $\bar{\omega}_-$ and $\bar{\omega}_+$ represent the flapping and twisting mode respectively is displayed in Fig. 6. Moreover this difference is plotted, for a fixed μ_2, as a function of $\bar{\omega}_3$ and μ_3. The two yellow lines represent the manufacturing limit values that can be reached by $\bar{\omega}_2$.

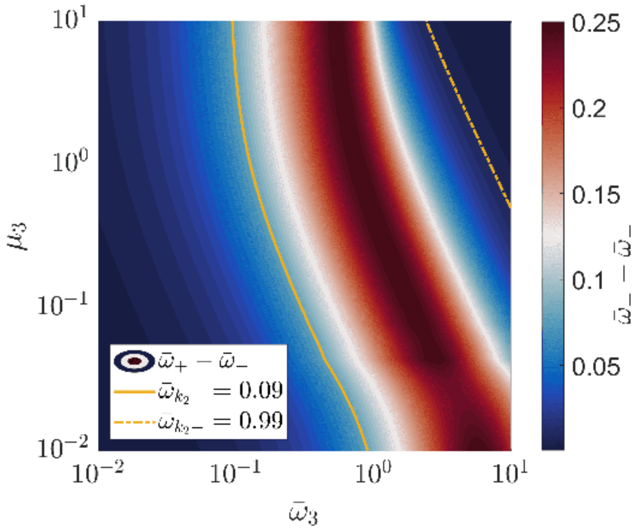

Fig. 6. Difference between the dimensionless pulsations of the first mode ($\bar{\omega}_-$) and the second mode ($\bar{\omega}_+$), displayed for the optimal $\bar{\omega}_2$ as a function of $\bar{\omega}_3$ and μ_3, with $\mu_2 = 0.01$. The solid line corresponds to $\bar{\omega}_{k_2-} = 0.09$, whereas the dash-dot line represents $\bar{\omega}_{k_2-} = 0.99$

The main conclusion of the study is that the condition $\mu_2 \ll 1$ must be respected in order to have a maximal amplitude at the phase quadrature frequency. Since the optimal $\bar{\omega}_2$ depends on the two parameters $\bar{\omega}_3$ and μ_3, we need to select on the Fig. 6 a point ($\bar{\omega}_3$, μ_3) lying in the gathered blue zone between the two yellow lines ($\bar{\omega}_{k_2-} = 0.09$ and $\bar{\omega}_{k_2-} = 0.99$), if we want to bring the flapping and twisting modes close enough.

IV. EXPERIMENTAL RESULTS

Once an optimal NAV geometry has been obtained using the 0D model, several prototypes have been manufactured using microfabrication technologies [16], [17]. More precisely, the fabrication principle was based on the used resin photosensitive characteristic, in this case the SU-8 resin. The NAVs have been manufactured on 3 inch diameter silicon wafers, on which around ten NAVs can be placed. At the beginning of the manufacturing process, an aluminium sacrificial layer was applied, onto which successive layers of SU-8 ranging between 15 µm and 200 µm were then deposited. After the development of the SU-8, Parylene C was pulverized onto the wafer to form the NAV's wings, which are thin membranes of 400 nm.

To demonstrate that significant angular displacements can be achieved with a compliant link system, a first prototype (Fig. 7) was built, with only a leading edge and no membrane. The tests on this prototype involved measuring its mode shapes and resonance frequencies. This allowed us to compare them with values obtained through finite element analysis, and therefore to validate the dimensioning method. Additionally, the prototype was then excited at the flapping frequency to measure the maximum angle achievable by the leading edge.

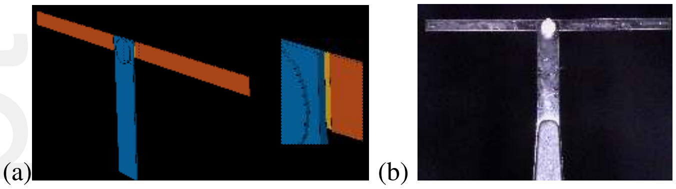

Fig. 7. Prototype with leading edge and no membrane (a) in simulation (b) after microfabrication

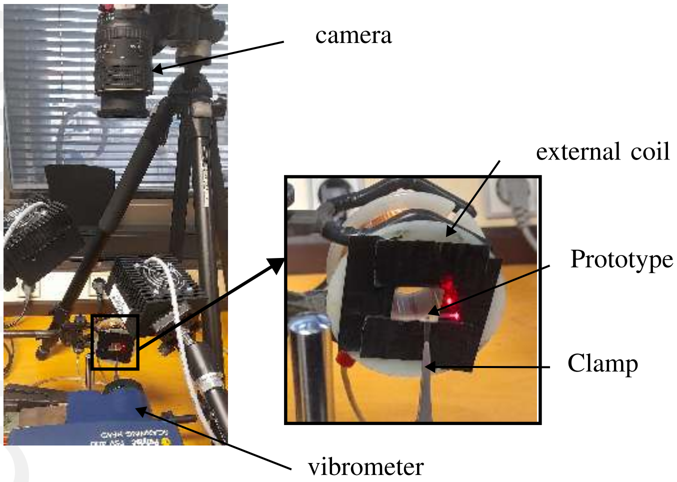

Fig. 8. Experimental set up with an external coil

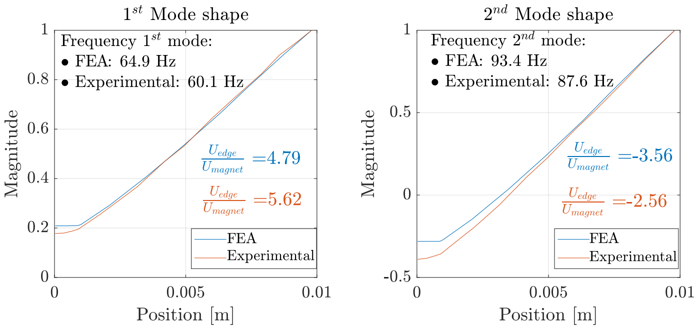

Fig. 9. Comparison between numerical simulations in blue and experimental measurements in red for a prototype with only a leading edge mode

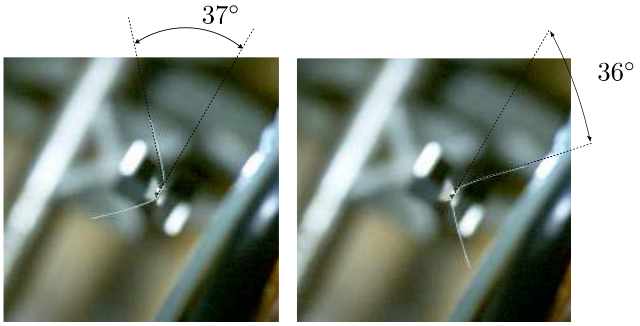

Fig. 10. Large-amplitude movement of a prototype with only leading edge and no membrane

In order to estimate the vibration modes of the NAV, a Polytec PSV-400 scanning laser vibrometer (Fig. 8) has been placed in front of the prototype, which is fixed by a clamp at the origin of its central beam and powered with an external coil (zoom in Fig. 8). More precisely, the scanning laser vibrometer can measure low-amplitude velocity at multiple points on the NAV when excited by a sinusoidal sweep. The FRF at each measurement point has been obtained by dividing the velocity measurement by the current introduced into the coil to excite the prototype. The experimental measurements are compared in Fig. 9 with the numerical values obtained by FEA analysis. Note that there are 7% errors in mode frequencies between the experiment and the simulation. The deformation amplitudes are compared using the ratio between the amplitude at the end of the leading edge and those at the magnet. Even though the correlation is acceptable, the error between the two ratios is greater than for the frequencies. This difference is attributed to a slight deformation of the leading edge, which remains straight in the simulation.

Once the flapping frequency has been identified using a scanning laser vibrometer measurement, amplitude tests have been carried out. The high-speed camera placed above the drone Fig. 8 enables at the same time to decompose the movement and to measure the obtained angles. As shown in Fig. 10, angles with amplitudes between $[36° - 37°]$ were measured. This validates the design of the compliant link, which not only achieves large deformation angles, but also gives results close to those simulated.

A prototype with trailing edge and leading edge without membrane has been then built to confirm that the dimension methodology is also valid for whole structures. A scanning laser vibrometer test was conducted, and Fig. 11 presents the comparison between experimental (in red) and numerical (in blue) FRF. Three points have been examined: the magnet (dot line), providing insight into the excitation amplitude, and the free ends of both the trailing (dashed line) and leading (solid line) edges. Notably, a strong correlation in frequencies and amplitudes was observed for the leading edge. The difference between the amplitudes can be attributed to the laser measurement point not being precisely at the free end of the rib and variations in damping created by air contact, which differs between the trailing and leading edges. Finally, a prototype with membrane, trailing edge and leading edge was designed, simulated and manufactured. High-amplitude quadrature motion was obtained, as shown by the high-speed camera images in Fig. 12.

V. CONCLUSION AND PERSPECTIVES

The goal of this work is to present a new design and microfabrication of a bioinspired (NAV). As compared to previous fully flexible designs, we localize the compliance in small elastic regions connected to rigid bodies, which enables to model the complete structure as a three degrees of freedom (0D) mass / spring system, provided that geometric criteria for the compliant links are respected. This simplifies the

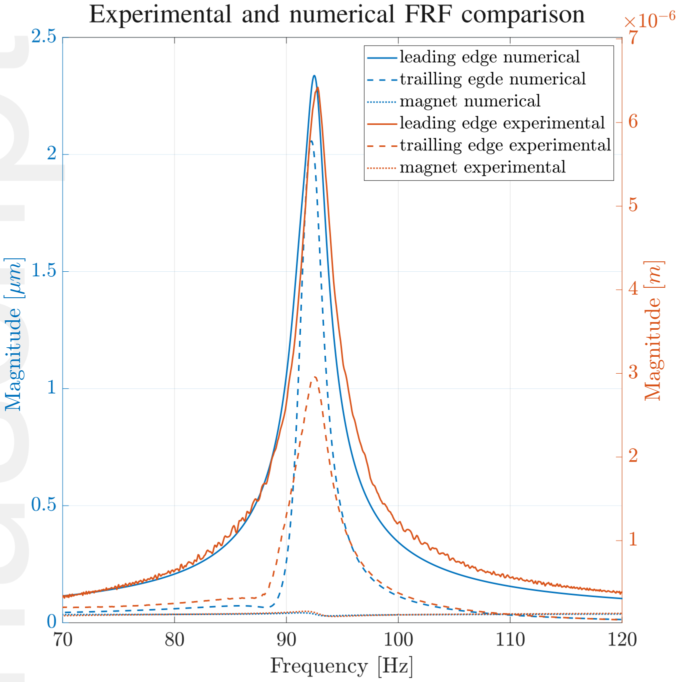

Fig. 11. Experimental (in red) and numerical (in blue) Frequency Response Functions (FRF) of a prototype with both leading and trailing edges, without a membrane. The solid line represents the free end of the leading edge, the dashed line corresponds to the trailing edge, and the dotted line indicates the magnet

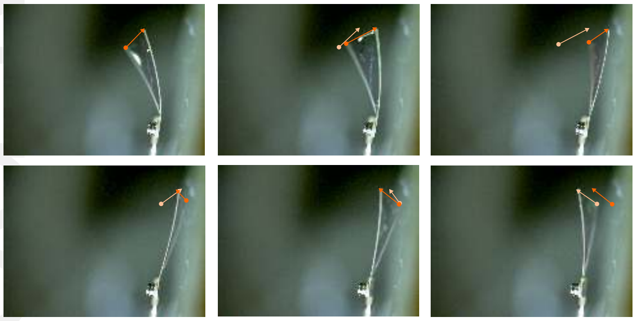

Fig. 12. Phase quadrature on the wing of a prototype with membrane, leading and trailing edges

optimization process, allowing us to optimize a NAV with only three parameters fixed by fabrication criteria and the actuator. This new design also enables to obtain very high vibration amplitude without damaging the structure. The result is prototypes, manufactured using microfabrication technologies, capable of producing large-amplitude wing motions of the order of 37° angle, but also able of being driven in their flapping and twisting modes independently or in phase quadrature. Finally, excellent correlation with theory is achieved, with less than 10% error on resonance frequencies and equivalent deformations. This validates the new used design strategy for a NAV weighing less than 40 mg and with a wingspan of less than 3 cm.

ACKNOWLEDGMENT

This work was supported by ANR-ASTRID NANOFLY (ANR-19-ASTR-0023), and the French AID (Defense Innovation Agency).

REFERENCES

[1] R. Srygley, A. Thomas, Unconventional lift-generating mechanisms in free-flying butterflies, Nature 420 (2003) 660–4.

[2] R. J. Wootton, The functional morphology of the wings of odonata, Vol. 5, 1991, pp. 153–169.

[3] M. Dickinson, F. Muijres, The aerodynamics and control of free flight manoeuvres in drosophila, Philosophical Transactions of the Royal Society of London. Series B, Biological Sciences 371 (09 2016).

[4] S. Ansari, K. Knowles, Insectlike flapping wings in the hover part i: Effect of wing kinematics, Journal of Aircraft - J AIRCRAFT 45 (2008) 1945–1954.

[5] C. Ellington, The novel aerodynamics of insect flight: applications to micro-air vehicles, Journal of Experimental Biology 202 (23) (1999) 3439–3448.

[6] X. Shengjie, K. Hu, B. Huang, H. Deng, X. Ding, A review of research on the mechanical design of hoverable flapping wing micro-air vehicles, Journal of Bionic Engineering 18 (11 2021).

[7] L. Petricca, P. Ohlckers, C. Grinde, Micro- and nano-air vehicles: State of the art, International Journal of Aerospace Engineering 2011 (01 2011).

[8] Y. Zou, W. Zhang, S. Zhou, X. Ke, F. Cui, W. Liu, Monolithic fabrication of an insect-scale self-lifting flapping-wing robot, Micro & Nano Letters 13 (2) (2018) 267–269.

[9] R. Wood, Liftoff of a 60mg flapping-wing mav, IEEE, 2007, pp. 1889 – 1894.

[10] K. Meng, W. Zhang, W. Chen, H. Li, P. Chi, C. Zou, X. Wu, F. Cui, W. Liu, J. Chen, The design and micromachining of an electromagnetic mems flapping-wing micro air vehicle, Microsystem Technologies 18 (12 2012).

[11] Rashmikant., D. Ishihara, Iterative design window search for polymer micromachined flapping-wing nano air vehicles using nonlinear dynamic analysis, International Journal of Mechanics and Materials in Design 19 (01 2023).

[12] D. Faux, O. Thomas, S. Grondel, E. Cattan, Dynamic simulation and optimization of artificial insect-sized flapping wings for a bioinspired kinematics using a two resonant vibration modes combination, Journal of Sound and Vibration 460 (2019).

[13] M. Colin, Conception d'un nano-drone ‘a ailes vibrantes, Ph.D. thesis, ´Ecole Nationale Sup´erieure d'Arts et M´etiers (06 2021).

[14] L. L. Howell, Compliant Mechanisms, John Wiley and Sons, 2001.

[15] Faux, D., Thomas, O., Cattan, É., and Grondel, S, Two modes resonant combined motion for insect wings kinematics reproduction and lift generation, EPL 121.6, 2018.

[16] X. Q. Bao, A. Bontemps, S. Grondel, E. Cattan, Design and fabrication of insect-inspired composite wings for mav application using mems technology, Journal of Micromechanics and Microengineering 21 (12) (2011) 125020.

[17] T. Dargent, X. Bao, S. Grondel, G. Brun, J. Paquet, C. Soyer, E. Cattan, Micromachining of an su-8 flapping-wing flying micro-electro-mechanical system, Journal of Micromechanics and Microengineering 19 (2009) 085028.

[18] M. Géradin, et D. J. Rixen (1994). Mechanical Vibrations: Theory and application to structural dynamics. Wiley. 617 p. (cf. p. 22-23, 230).